ACS OMEGA

http://pubs.acs.org/journal/acsodf

Article

G2/M-Phase-Inhibitory Mitochondrial-Depolarizing Re(I)/Ru(II)/Ir(III)-2,2′-Bipyrimidine-Based Heterobimetallic Luminescent Complexes: An Assessment of In Vitro Antiproliferative Activity and Bioimaging for Targeted Therapy toward Human TNBC Cells

Nilmadhab Roy,[‖] Shanooja Shanavas,[‖] Binoy Kar,[‖] Lavanya Thilak Babu, Utpal Das, Seshu Vardhan, Suban K. Sahoo, Bipasha Bose,* Vijayaraghavan Rajagopalan,* and Priyankar Paira*

Cite This: *ACS Omega* 2023, 8, 12283−12297

Read Online

ACCESS | Metrics & More | Article Recommendations | Supporting Information

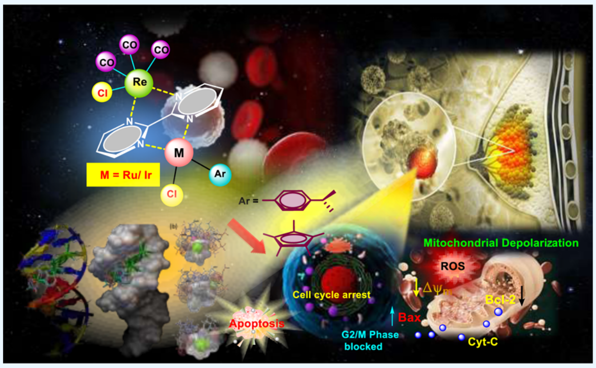

ABSTRACT: Triple-negative breast cancer (TNBC) is an extremely vicious subtype of human breast cancer having the worst prognosis along with strong invasive and metastatic competency. Hence, it can easily invade into blood vessels, and presently, no targeted therapeutic approach is available to annihilate this type of cancer. Metal complexes have successfully stepped into the anticancer research and are now being applauded due to their anticancer potency after the discovery of cisplatin. Many of these metal complexes are also well recognized for their activity toward breast cancer. As the TNBC is a very dangerous subtype and has long been a challenging ailment to treat, we have intended to develop a few brand new mixed metallic Ru(II)/Ir(III)/Re(I)-2,2′-bipyrimidine complexes [**L′Re2**], [**L′RuRe**], and [**L′IrRe**] to abate the unbridled proliferation of TNBC cells. The potency of the complexes against TNBC cells has been justified using MDA-MB-468 TNBC cell lines where complex [**L′IrRe**] has displayed significant potency among all the three complexes with an IC_{50} value of 24.12 μM. The complex [**L′IrRe**] has been competent to cause apoptosis of TNBC cells through inhibition of the G2/M phase in the cell cycle in association with a profuse amount of ROS generation and mitochondrial depolarization.

■ INTRODUCTION

Breast cancer (BC) is the most pernicious type of cancer and has been ascribed as the second most prime cause of premature mortality among women. Around 1.5 million women (20−59 years) throughout the world and in the Middle East part of the globe are being the victims of this cancer in each year as per global cancer project (GLOBOCAN 2012).[1,2] Of note, it has been observed that the female in less developed and in industry-based countries encounters the most common non-dermatologic malignancy, and thus, it has been unveiled as a second vital reason of mortality in the United States and in Europe after lung cancer.[3,4] The steady increase in global encumbrance of BC in all ethnicities can be assumed to prevail due to the exogenous factors like lifestyle, reproductive factors, and genetic factors like mutations occurring in breast cancer susceptibility gene 1 (BRCA1) and breast cancer susceptibility gene 2 (BRCA2), manifesting the tumors with more hostile phenotypes and thereby playing a significant role in the etiology of such cancer.[5] The high body mass index (BMI), family history of ovarian or breast cancer, nulliparity or first birth at age greater than 30, late menopause, and postmenopausal hormone therapy can be included as the other most important risk factors of breast cancer.[6] There are four subtypes of breast cancer which are allied with unambiguous histologies and specific prognoses and have been classified depending on its anatomical origin (lobular or ductal), hormone receptivity, and the expression of human epidermal growth factor receptor 2 (HER-2), CK5/6, vascular endothelial growth factor (VEGF), and KI67.[7] Estrogen receptor alpha (ERα) and progesterone receptor (PR) have also been recognized as the key biomarkers in most of the common subtypes of breast cancer along with the human epidermal growth factor receptor2 (HER-2) biomarker.[8] However, the triple-negative breast cancer (TNBC) subtype which is further categorized into A (luminal-like) and B (basal-like) lacks in the existence of ER, PR, and HER-2 biomarkers, and for this very cause, TNBC has been identified as a highly

Received: December 30, 2022
Accepted: January 30, 2023
Published: March 21, 2023

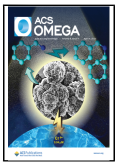

aggressive breast cancer among all subtypes owing to its very poor prognoses, high rate of distant metastasis (brain, lungs, bone, and liver), increased risk of relapse, and lack of specific molecular targets along with a higher rate of recurrence.[9] Also, TNBC is being assumed to be the most challenging disease to treat due to its heterogeneity and complexity. Therefore, it has been a matter of great woe for the TNBC-riddled patient as TNBC is insensitive to modern therapies.[10,11] In order to heal TNBC, surgery, radiation therapy, and chemotherapy are now being applied in a combined way where chemotherapy is assumed to be the best among all the prevailing therapies to care for metastasis of various types of cancer.[12] However, the inadequate affectivity of present systemic and targeted therapies deserves the further research in finding out a different strategy of treatment to perk up the patient prognosis. The therapeutic potential of metal complexes is very well known from long before, and in recent time, metal complexes have been giving away ample evidence as potential candidates for cancer therapies.[13] The first metal-based complex, cisplatin, established the pillar of anticancer research, and it showed its anticancer activity through apoptotic mechanisms.[14] Although cisplatin can exert a significant effect on TNBC cells having BRCA deficiency, the profuse shortcomings of cisplatin and its analogues compelled the researchers to engross into plenty of investigations for developing non-platinum-based metal complexes which will be capable of resisting both cancer cell proliferation and metastasis.[15] In this regard, some astounding properties of ruthenium, iridium, and rhenium metals have been recognized for designing excellent anticancer agents during the last few years. Ruthenium complexes are very much prospective for inhibition of growth of various cancer cells such as breast, ovarian, and melanoma.[16] Shriver et al. constructed ruthenium complex of *o*-phenylene diamine (*o*-PDA) which adeptly hindered the growth of breast cancer (BC) such as MDA-MB-231, SKBR-3, and SUM149, but it was incapable of inhibiting the growth of human breast epithelial cells (MCF-7). It was noticed that the growth of MDA-MB-231 cells was inhibited by the treatment of the *o*-PDA complex by significantly reducing the production of growth regulatory proteins such as VEGF-A, GM-CSF, and PDGF-AA at the transcriptional level.[17] The antitumor and antimetastatic properties of ruthenium complexes have been again justified by Cominetti et al. by developing a series of biphosphine, bipyridine Ru-complexes, $[\mathrm{Ru(SO_4)(dppb)(bipy)}]$, $[\mathrm{Ru(CO)_3(dppb)(bipy)}]$, $\mathrm{Ru(C_2O_4)(dppb)(bipy)}]$, and $[\mathrm{Ru(CH_3CO_2)(dppb)(bipy)}]\mathrm{PF_6}$ (dppb = 1,4-bis(diphenylphosphino)butane, bipy = 2,2′-bipyridine), and representing their potential against the proliferation of TNBC (MDA-MB-231) and estrogen-positive (ER+) breast tumor cells (MCF-7).[18] Chen et al. designed a group of Ru-polypyridyl complexes which explored their anti-breast cancer activity, triggering the natural killer cell (NK)-mediated immunotherapy against MDA-MB-231 cells.[19] Batista and his research group also established a few Ru (II)-diphosphine complexes which were very competent to exhibit their anticancer activities against MDA-MB-231 TNBC cells.[20] Iridium(III) complexes have also drawn the interest in anticancer therapy due to their versatile photophysical properties along with limited side effects. Leung et al. studied the apoptotic cell death capability of various Ir(III) complexes.[21] Sadler et al. synthesized half-sandwich cyclopentadienyl (Cp*) Ir (III) complexes and evaluated their mechanism of action (MoA) in cancer cells.[22] Lu et al. showed the anti-breast cancer tumorigenesis and metastasis activity of sulfur-coordinated organoiridium (III) complexes containing C, N and S, S chelating ligands by targeting the Wnt/β-catenin signaling pathway where the complexes triggered the dilapidation of LRP6, diminishing the protein levels of DVL2 (β-catenin and activated β-catenin), along with the down-regulation of Wnt target genes CD44 and survivin.[23] Ir(III) complexes can perturb the cellular redox balance which in turn causes lipid peroxidation and ferroptosis in cancer cells and thereby triggers the immunogenic cell death (ICD).[24] On the other hand, rhenium-based metal complexes are enthralling the mind of the researchers due to their incredible physicochemical properties which enable them to be used in cancer therapy. In this regard, carbonyl complexes of rhenium are noteworthy for cancer therapy. Rhenium(I) tricarbonyl complexes have shown remarkable properties which are applicable for biomedical applications such as bioimaging and healing of cancer.[25] $\mathrm{Re(I)(CO)_3^+}$ complexes display polarized emission, high photostability, large Stokes shift, and long lifetimes.[26] Not only Re(I) possesses d^6 electronic configuration in its outermost shell but also it possesses high biocompatibility. Therefore, d^6 configuration makes the Re(I) tricarbonyl complexes kinetically inert, which helps to circumvent heavy metal-related toxicity.[27] These complexes are also suitable for showing photocytotoxic activity and photosensitizing ability. Perera et al. synthesized a novel Re(I) tricarbonyl complex having piperidinyl sulfonamide ligands. It has been seen that Re(I) tricarbonyl complexes are efficient to take part in ligand exchange kinetics as that of the same order of platinum-based drugs. However, Re(I) complexes are superior to platinum-based anticancer agents for their outstanding spectroscopic properties which obligate them to be employed in imaging.[28] Re(I) tricarbonyl complexes exhibit triplet-state luminescent emission along with their distinct $\mathrm{C{\equiv}O}$ stretching frequency, which affords the imaging efficiency by vibrational microscopy. In addition to this, Wilson et al. developed a few Re(I) tricarbonyl aqua complexes with 2,2′-bipyridine derivatives which were affluent in leveraging intrinsic luminescent properties and production of reactive oxygen species (ROS) along with the depolarization of mitochondrial membrane potential after substantial intracellular localization.[29] Schindler and Zobi developed various Re(I) di- and tri-carbonyl anticancer complexes with several structural variations.[30] In association with the variation of Ru(II), Ir(III), and Re(I) metals, the incorporation of bioactive ligands has gained considerable attention owing to its multitargeting properties. In this regard, the work of Isab and co-workers showed that the incorporation of bipyridine and bipyrimidine ligands with Au (III) metals introduced a number of MoAs which include inhibition of thioredoxin reductase (TrxR), inhibition of proteasome, generation of ROS, modulation of kinases, DNA intercalation, and obstruction in MCF-7 cell cycle phases.[31] Moreover, the heterocyclic pyrimidine is the part and parcel of DNA and RNA enriched with varied pharmacological properties along with good water solubility. Therefore, Kumar and Narasimhan et al. studied the therapeutic potential of pyrimidine scaffolds flourished with a broader range of biological activities such as anticancer, antioxidant, antiviral, anti-inflammatory, antimicrobial, analgesic, antimalarial, and so forth.[32] The study of structure−activity relationship (SAR) of pyrimidine derivatives enlightened that this moiety was very promising for anticancer activity, triggering the upregulation of Bax and downregulation of Bcl-xl proteins in association with

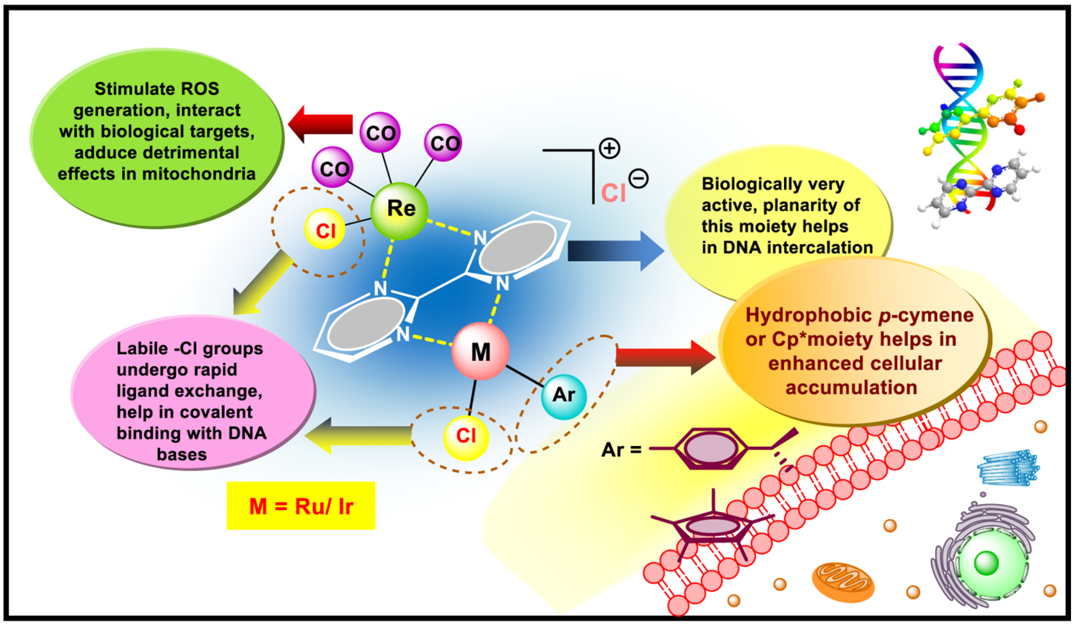

Figure 1. Design of 2,2′-bypyrimidine-based heterobinuclear luminescent Ru(II)/Ir(III) and Re(I) complexes.

Scheme 1. Synthetic Route for Homo- and Heterobinuclear Ru(II), Ir(III), and Re(I) 2,2′-Bipyrimidine Complexes [L′Re2], [L′RuRe], and [L′IrRe]

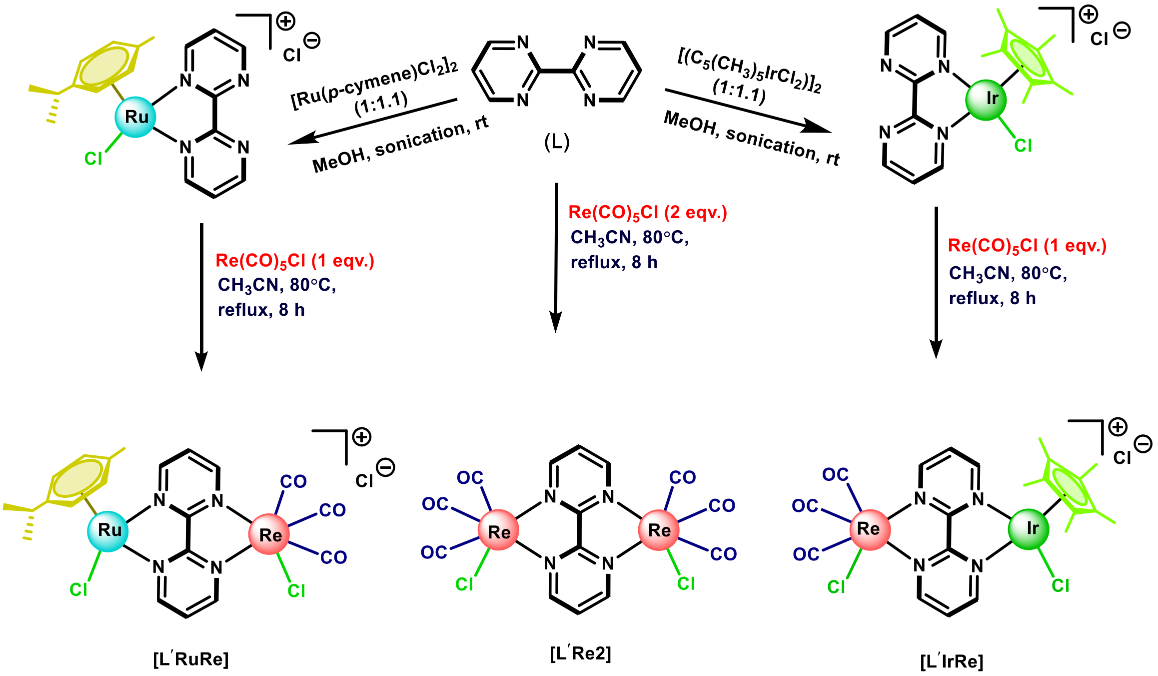

the blockage of the G2-M phase of the cell cycle.[33] Furthermore, it has been perceived that the pyrimidine moiety is accountable to control the transcription factors and polymerases where the drug molecule will be adequate to interact with protein bound to DNA. Another important facet of the pyrimidine moiety is the capability of non-covalent binding of small molecules to the DNA double-stranded structure either by intercalation or through interaction with the minor groove of nucleic acids along with the binding efficacy to topoisomerase IIα (Topo IIα) in coordination with DNA.[34]

Therefore, bearing all the benefits of ruthenium, iridium, and rhenium metals and the pyrimidine moiety in mind, the present work aims to develop well-characterized Re (I)/Ru(II)/Ir(III)-2,2′-bipyrimidine-based bimetallic complexes being endowed with all palpable properties worthy of healing the TNBC (Figure 1). The potency of synthesized complexes has been vindicated against MDA-MB-468 TNBC cells and one normal immortalized human keratinocyte cell line HaCaT.

■ RESULTS AND DISCUSSION

Chemistry. *Synthesis and Characterization.* The synthetic procedure of three bimetallic complexes [**L′Re2**], [**L′RuRe**], and [**L′IrRe**] has been portrayed in Scheme 1. First, homobinuclear Re(I) complex [**L′Re2**] was prepared by

Table 1. Photophysical Characterization, Lipophilicity, and Conductivity Study of the Complexes [**L′Re2**], [**L′RuRe**], and [**L′IrRe**]

	λ_a (nm)[a]							Λ_M (S m^2M^{-1})[g]	
samples	$\pi-\pi^*$	MLCT	λ_f (nm)[b]	O.D[c]	ε (M^{-1} cm^{-1})[d]	(ϕ_f)[e]	log $P_{o/w}$[f]	DMSO	10% DMSO
[**L′Re$_2$**]	305		366	1.23	41,000	0.0143	0.220	14	140
[**L′RuRe**]	306	∼400	369	1.47	49,000	0.0095	0.2415	23	190
[**L′IrRe**]	304	∼400	371	1.78	59,333	0.0077	0.4704	32	195
quinine sulfate	350	452	0.26	8000	0.546				

[a] Absorption maxima. [b] Emission wavelength. [c] Optical density. [d] Extinction coefficient. [e] Quantum yield. [f] *n*-Octanol/water partition coefficient. [g] Conductance in DMSO and 10% aqueous DMSO.

mixing the 2,2′-bipyrimidine ligand (**L′**) with $Re(CO)_5Cl$ in a 1:2 ratio and keeping the reaction mixture under reflux at 80 °C for 8 h. The progress of the reaction was monitored time to time by thin-layer chromatography (TLC). After completion of the reaction, the solvent was evaporated by a rotary evaporator, and the reddish-brown colored crude product was obtained. Then, the crude product was washed repeatedly with hexane and recrystallized from the diethyl ether/methanol mixture to remove the impurities. As a result, reddish-brown crystalline homobinuclear Re(I) complex [**L′Re2**] was obtained with high yield (95%). The structure of [**L′Re2**] was then scrutinized by ^1H and ^{13}C NMR spectroscopy, FT-IR spectroscopy, and high-resolution mass spectrometry (HRMS). The ^1H NMR spectrum of complex [**L′Re2**] showed that four most deshielded protons appeared as multiplet (m) at δ 9.33−9.36 ppm in the downfield region and two protons appeared as triplet (t) at δ 7.93 ppm. The incorporation of Re(I) was confirmed from the characteristic peak of the CO group at δ 197.2 ppm in the ^{13}C NMR spectrum. In order to synthesize binuclear mixed metallic complexes [**L′RuRe**] and [**L′IrRe**], the precursor Ru(II) and Ir(III) mononuclear complexes of the 2,2′-bipyrimidine ligand (**L′**), namely, [(η6-*p*-cymene)RuCl(bipyrimidine)][**L′Ru**] and [(η5-Cp*)IrCl(bipyrimidine)][**L′Ir**], were synthesized and then characterized following the previous method reported by our group (Scheme 1).[35] After that, the mononuclear complexes [**L′Ru**] and [**L′Ir**] were dissolved in an acetonitrile solvent, and 1 equiv of $Re(CO)_5Cl$ was added to the reaction media. Then, the clear reaction mixtures were refluxed for 8 h at 80 °C. The progress of the reaction was monitored by TLC. After the completion of the reaction, the solvent was evaporated and the crude products of heterobinuclear complexes [**L′RuRe**] and [**L′IrRe**] were washed thoroughly with hexane and then recrystallized from the diethyl ether/methanol mixture to remove the impurities. Finally, we obtained dark red colored [**L′RuRe**] and yellow colored [**L′IrRe**] crystalline complexes with high yield (92−96%). The structures of the two complexes [**L′RuRe**] and [**L′IrRe**] were authenticated by ^1H and ^{13}C NMR spectroscopy, FT-IR spectroscopy, and HRMS. In ^1H NMR spectroscopic analysis, the two most deshielded protons appeared as doublet (d) at δ 9.57 ppm and other four protons appeared as multiplet (m) at δ 8.04−8.08 ppm in the case of complex [**L′RuRe**]. The methyl protons of the *p*-cymene ring appeared in the range of δ 1.20 ppm as doublet. The six CH_3 protons of the isopropyl group appeared as singlet at δ 2.15 ppm. Likewise, CH protons of the isopropyl group were found as multiplet in the region of δ 2.81−2.88 ppm. The four aromatic protons of *p*-cymene rings appeared in the region of δ 6.08−6.32 ppm. In the ^{13}C NMR spectrum, the characteristic peak of the CO group was visualized at δ197.2 ppm, which ensured the attachment of Re (I) metal holding three CO groups. The C=O stretching at 1884 cm^{-1}, aromatic C=C stretching at 1578 cm^{-1}, C−N stretching at 1410 cm^{-1}, C−H stretching at 1146 cm^{-1}, and C−H bending at 733 cm^{-1} appeared in the IR spectrum for complex [**L′RuRe**]. In the case of complex [**L′IrRe**], the most downfielded three protons appeared as multiplet (m) at δ 9.32−9.36 ppm, one proton appeared as triplet (t) at δ 8.05 ppm, and other two protons at δ 7.93 ppm appeared as triplet in association with the appearance of a characteristic peak for 15 Cp* protons at δ 1.62 ppm in the ^1H NMR spectrum. The characteristic peak of the CO group was observed at δ 197.5 ppm, indicating the coordination of Re(I) bearing three CO groups. In the FT-IR spectrum, stretching frequency for C=O was observed at 1896 cm^{-1} along with aromatic C=C stretching at 1578 cm^{-1}, 1410 C−N stretching at 1410 cm^{-1}, C−H stretching at 1020 cm^{-1}, and C−H bending at 733 cm^{-1}. The HRMS peak at *m*/*z*: 770.5486 $[M + H]^+$, 734.5915 $[M{-}Cl]^+$, and 826.7466 $[M{-}Cl]^+$ confirmed the formation of complexes [**L′Re2**], [**L′RuRe**], and [**L′IrRe**], respectively.

Physicochemical Studies. Electronic Absorption (UV−Visible) and Fluorescence Study. In order to unearth the cellular imaging properties of synthesized complexes [**L′Re2**], [**L′RuRe**], and [**L′IrRe**], UV−visible and fluorescence studies were accomplished in the (1:9 v/v) dimethyl sulfoxide (DMSO): water mixture and in the acetonitrile−water mixture (Figures S14 and S15). The UV−visible spectral analysis conveyed that these complexes were competent to display strong absorption bands in the range of 275−375 nm in aqueous DMSO medium, whereas in the range of 250−350 nm in aqueous acetonitrile medium, indicating the characteristic intraligand (N̂N) charge transfer (LLCT) transitions. However, the absorption bands due to metal to ligand charge transfer (MLCT) in the higher wavelength region were observed insignificantly (λ_{abs} ∼ 400 nm). The appearance of highly intense absorption bands in the lower wavelength region was due to the charge transfer between the lower energy π-bonding highest occupied molecular orbital (HOMO) to the higher energy lowest unoccupied π^*-antibonding molecular orbital (LUMO) of the ligand, that is, the $\pi-\pi^*$ transition led to the exposition of these highly intense absorption bands in the lower wavelength region. It was apparent that complex [**L′IrRe**] displayed the absorption with the highest intensity among all the three complexes (Figure S13). In fluorescence spectra, it was observed that the complexes [**L′Re2**], [**L′RuRe**], and [**L′IrRe**] divulged the emission in the range of 320−560 nm as a result of LLCT by electronic transition from the higher energy π^*-molecular orbital to the lower energy π-molecular orbital of the ligand after exciting the molecules at around 280 nm. The complex [**L′Re2**] showed the best LLCT emission at a λ_{ems} of 380 nm with the highest intensity (Figure S14). From the emission spectral profile, the

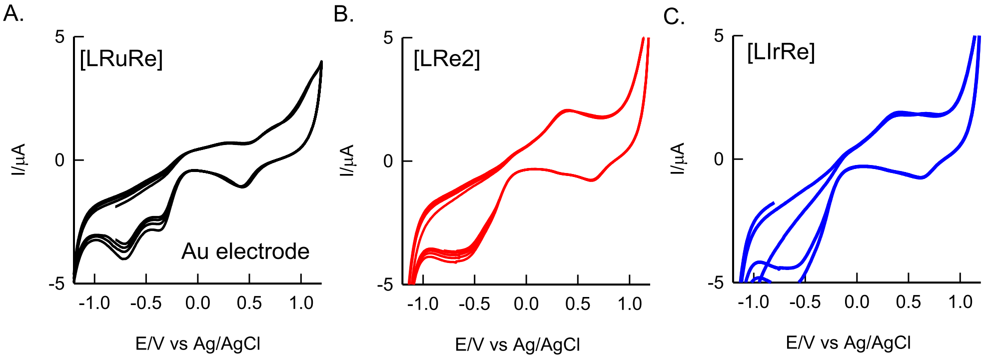

Figure 2. Cyclic voltammetry response of (A) [**LRuRe**], (B) [**LRe2**], and (C) [**LIrRe**] at the potential window of (−1.2 to 1.2) V vs Ag/AgCl in 0.1 M sodium sulfate solution at a scan rate of 50 mV s^{-1}.

corresponding quantum yields (Φ_f) of three complexes were calculated from equation (ii) (Table 1). It was found that three complexes were significantly fluorescent, acquiring the ability of photocytotoxicity and cellular imaging. However, complex [**L′Re2**] exposed the highest quantum yield (Φ_f) of 0.0143 and thereby achieved the best luminescent property compared to other two complexes.

Solubility, Lipophilicity, and Conductivity Study. The equilibrium between lipophilicity and hydrophilicity is an essential aspect for establishing the tumor-shrinking potential of metal complexes. Therefore, the drug-like characteristics of the complexes can be well exposed with their lipid-bilayer-penetrating ability during cellular entry, that is, with the extent of their lipophilicity. It was seen that the homobimetallic complex, [**L′Re2**], and heterobimetallic complexes, [**L′RuRe**] and [**L′IrRe**], were highly soluble in DMSO and DMF and decently soluble in water, methanol, ethanol, and acetonitrile but feebly soluble in hydrocarbon solvents. The solubility of these complexes at 25 °C was in the range of 6−8 mg/mL DMSO-10% DMEM medium (1:99 v/v, comparable to cell media). In order to give insights into the lipophilic profile of complexes [**L′Re2**], [**L′RuRe**], and [**L′IrRe**], we determined the magnitude of n-octanol/water partition coefficient (log $P_{o/w}$, where $P_{o/w}$ = octanol/water partition coefficient) by means of the conventional shake-flask method (Table 1).[36] The investigational log $P_{o/w}$ values of these complexes were seen to be in the range of 0.22−0.47. The highest log $P_{o/w}$ value of the complex [**L′IrRe**] endorsed the significant accumulation of the complex in the mitochondria for the lipophilic effects of both Cp* and CO groups. The molar conductivity of these bimetallic complexes [**L′Re2**], [**L′RuRe**], and [**L′IrRe**] were observed as 14, 23, and 32 S cm2 mol^{-1}, respectively, in pure DMSO. On the other hand, a significant increase in the molar conductance values of all these complexes in 10% aqueous DMSO (140−195 S cm2 mol^{-1}, Table 1) indicated the dissociation of the M−Cl bond in the tested system, which confirmed the aqua complex formation in bulk aqueous medium.

Study of Electrochemical Properties. The cyclic voltammetry response of the complexes [**L′Re2**], [**L′RuRe**], and [**L′IrRe**] was recorded using a cleaned gold electrode as a working electrode. The gold electrodes were pretreated in a blank solution at the potential window of −0.2 to 1 V versus Ag/AgCl for the continuous cycles (n = 20). Then, the samples were dissolved in 0.1 M electrolytic solution of sodium sulfate at 1 mM concentration in a 10 mL glass container. To avoid the turbidity, 1 mL of ethanol was also spiked inside the prepared solution. The experiments were recorded using the Au electrode as the working electrode at the potential window of −1.2 to 1.2 V versus Ag/AgCl at a scan rate of 50 mV s^{-1}. The peak stability was retained even after multiple cycles of cyclic voltammetry (Figure 2). Hence, CV characterization unveiled the significant redox nature of the concerned complexes, indicating their high stability (Table 2).

Table 2. Electrochemical Data of Complexes [L′Re2], [L′RuRe], and [L′IrRe] in 0.1 M Na_2SO_4

s. no.	samples	$E^{o\prime}/V$ vs Ag/AgCl
1	[**L′RuRe**]	−0.701
2	[**L′Re2**]	−0.621
3	[**L′IrRe**]	−0.512

Theoretical Study. Density Functional Theory (DFT) Study. The DFT calculations were performed to predict the 3D structure of the complexes [**L′Re2**], [**L′RuRe**], and [**L′IrRe**]. The complexes were optimized in the gas phase by applying the exchange correlation functional B3LYP coded in the Gaussian 09W computational program.[37] The basis set 6-31G** was used for the C, O, Cl, and H atoms, whereas the LANL2DZ basis set was used for the metal atoms (Re, Ir, and Ru). The DFT computed structure of the complexes along with their important bond lengths are shown in Figure 3. Each metal center in the [**L′Re2**], [**L′RuRe**], and [**L′IrRe**] complexes preferred a pseudo-octahedral geometry. The Ru in the [**L′RuRe**] complex is coordinated to the p-cymene ring, whereas the five carbons of pentamethylcyclopentene are coordinated to Ir in the [**L′IrRe**] complex. The Ru-center and Ir-center formed a "three leg piano-stool" structure in their respective complexes [**L′RuRe**] and [**L′IrRe**]. The seat is formed by η^5-/η6-arene, and the two coordinate bonds with the biphenyl-C and one to a chloride atom formed the three legs of the stool. In [**L′RuRe**], the bond angles for the C−Ru−C and C−Ru−Cl are, respectively, 81.83 and 90.85°, and the distance from the Ru to six carbon atoms of the p-cymene ring is observed between 2.450 and 2.639 Å with an average distance of 2.779 Å. In [**L′IrRe**], the bond angles for the C−Ir−C and C−Ir−Cl are observed to be 80.91 and 87.77°, respectively, and the distance to five carbon atoms of pentamethylcyclopentene from Ir lies between 2.219 and 2.497 Å with an average distance of 2.365 Å. From the computed structure, the band gaps of the complexes were obtained as 0.08, 0.06, and 0.06 eV for [**L′Re2**], [**L′RuRe**], and [**L′IrRe**], respectively, which supported the internal

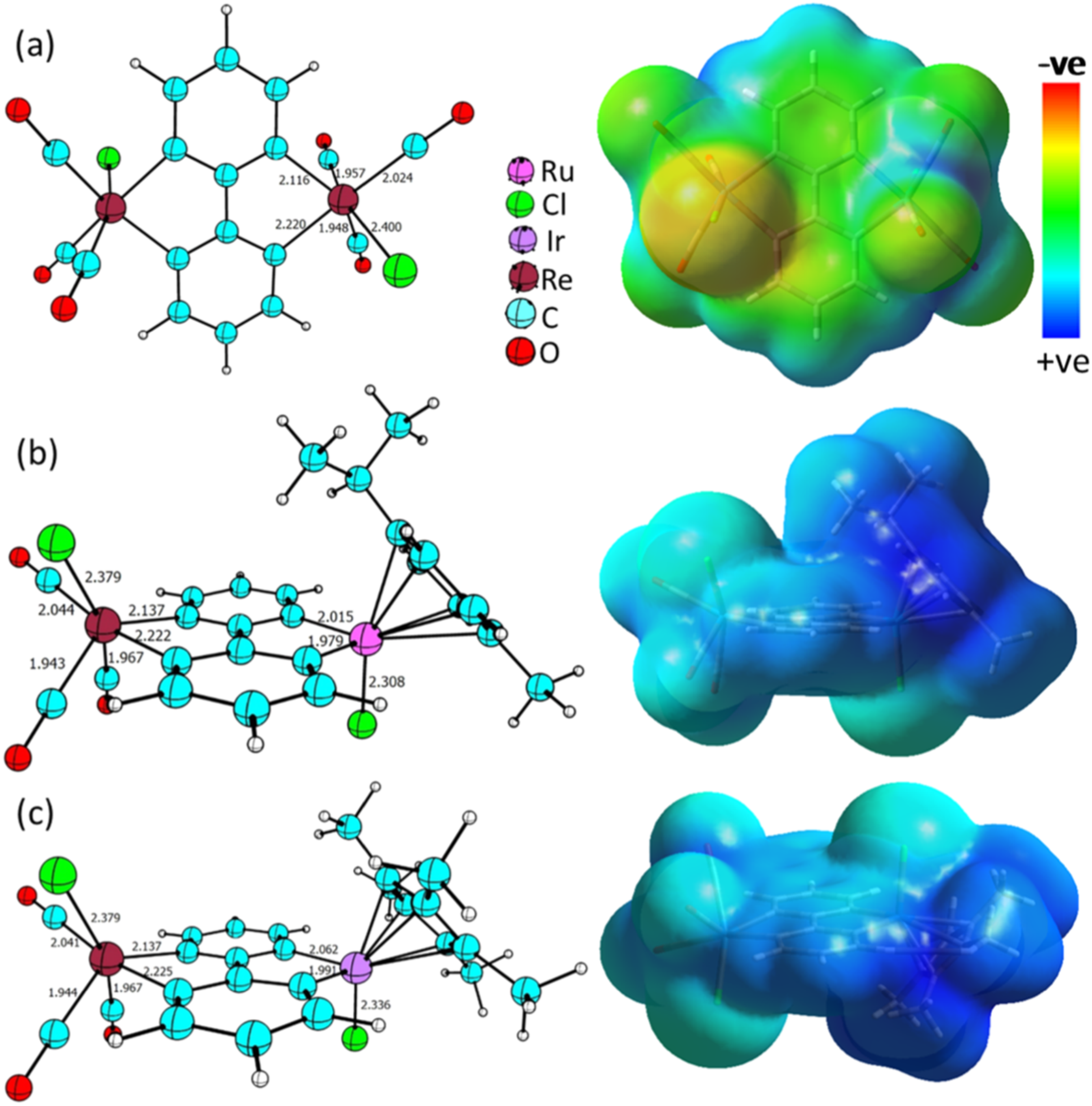

Figure 3. DFT (B3LYP/6-31G**/LANL2DZ)-computed structure of the complexes (a) [**L′Re2**], (b) [**L′RuRe**], and (c) [**L′IrRe**] and their molecular electrostatic map (MEP).

charge transfer that occurred in the [**L′RuRe**] and [**L′IrRe**] complexes upon replacing the Re atom with Ru/Ir. Analysis of the molecular electrostatic map (MEP) of the complexes supported the fact that internal charge transfer occurred in the complexes, where the red region showed the most negative region, while the positive region is shown in blue color (Figure 3). In [**L′Re2**], the red region is dominated, while the blue colored regions are dominated in the complexes [**L′RuRe**] and [**L′IrRe**].

Molecular Docking Study. The binding modes and affinity of the complexes were investigated with the bovine serum albumin (BSA) and DNA by performing the molecular docking experiments. The Autodock 4.2 computational program with the Lamarckian genetic algorithm (LGA) was used to study the docking experiments.[38] The crystal structures of DNA (PDB ID: 1BNA) and BSA (PDB ID: 4SFS) were downloaded from the Protein Data Bank, and the structures were refined by using the online tool Swiss model. The estimated free energy of binding and the inhibition constant (K_i) of the complexes with BSA and DNA are summarized in Table S1. The results in Table S1 revealed that the organometallics are showing similar binding affinity toward BSA and DNA. The [**L′RuRe**] complex showed a higher affinity with BSA, whereas the [**L′IrRe**] with DNA had a lower inhibition constant.

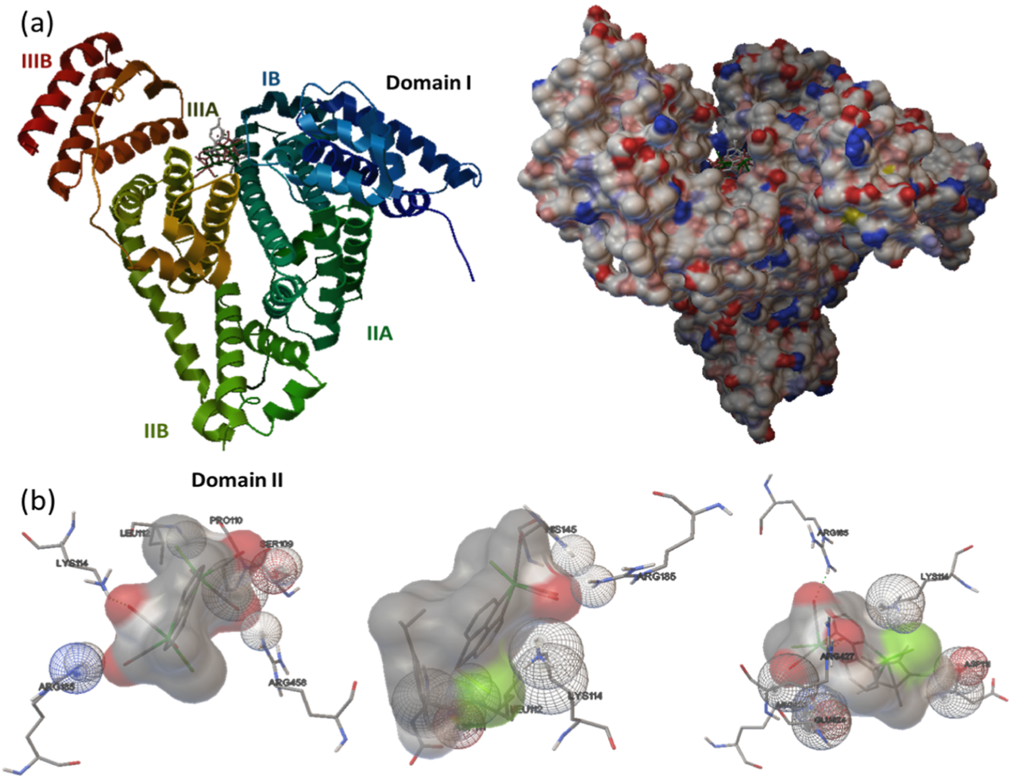

Figure 4. 3D views of the best pose of the complexes within the hydrophobic cavity of BSA (a). Interaction of different residues of BSA with the complexes (b).

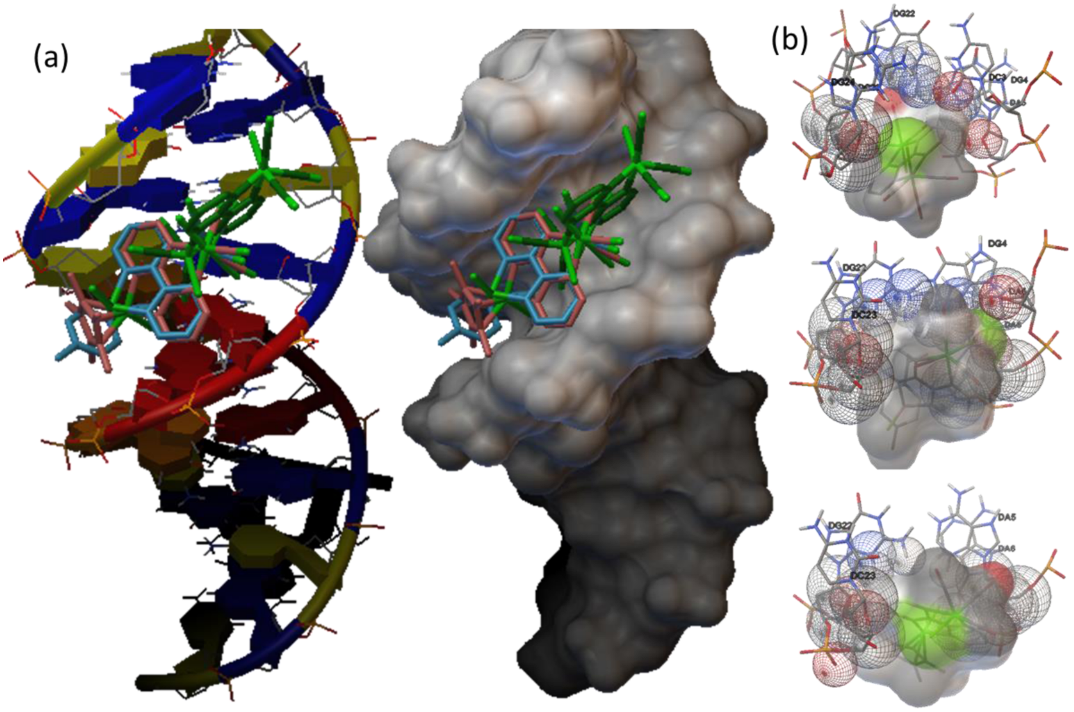

Figure 5. 3D views of the best pose of the complexes with the DNA (a). (b) Structure showing the important interactions between the complexes with DNA.

The blind docking of the complexes [**L′Re2**], [**L′RuRe**], and [**L′IrRe**] with BSA was performed by keeping the grid dimensions of x = 8.376, y = 21.661, and z = 106.639. The BSA with a molecular mass of 66,200 Da in a single polypeptide chain consists of 583 amino acid residues (Figure 4).[39] It contains three homologous domains (I, II, and III), and each domain is divided into two sub-domains, A and B. BSA showed intrinsic fluorescence due to the presence of two tryptophan (TRP) residues: the residue TRP212 is present within the hydrophobic binding pocket of subdomain IIA, whereas TRP-134 is present in domain I over the surface of the albumin. The main ligand binding sites in BSA are located in the subdomains IIA and IIIA. All the complexes bind between the domains II and III with a similar bind affinity (Figure 4a). The dock scores are found to be between −5.63 and −5.96 kcal/mol. As shown in Figure 4b, the docked structure is stabilized due to the multiple non-covalent interactions occurring between the complexes and the amino acid residues of the BSA protein. Similarly, Figure 5a shows the best pose of the metal complexes with DNA obtained after performing the docking experiments. The grid dimensions were adjusted by keeping x = 13.358, y = 20.325, and z = 10.766. All the complexes stacked at one place within the two chains of DNA by interacting with the major grove electrostatically. The estimated free energy of the complexes was observed between −5.56 and −5.76 kcal/mol. The base pairs of DNA are forming non-covalent interactions with the complexes and stabilize the docked structure (Figure 5b).

Biology. *Cytotoxicity Study.* The in vitro cytotoxicity of the complexes [**L′Re2**], [**L′RuRe**], and [**L′IrRe**] was evaluated by the MTT assay against MDA-MB-468 breast cancer cell lines. The specified cell line was incubated with the test compounds at various doses ranging from 5 to 500 μM for 48 h in vitro. The IC_{50} values of the test compounds in MDA-MB-468 breast cancer cell lines were found to be 104.56 ± 1.4, 110.98 ± 1.5, and 24.12 ± 1.1 μM, respectively, for [**L′Re2**], [**L′RuRe**], and [**L′IrRe**] (Figures S15 and S16). Consequently, the most potent compound among the series, [**L′IrRe**], was selected for further downstream experiments on the immortalized human keratinocyte cell line HaCaT (i.e., normal cell line). The IC_{50} value of [**L′IrRe**] on HaCaT was found to be 234.8 ± 2.4 μM, which is ∼10-fold higher than the IC_{50} value of the [**L′IrRe**] complex on the breast cancer cell line MDA-MB-468. The cell viability assays suggested the dose-dependent cytotoxic effects of the [**L′IrRe**] complex, on breast cancer cell line MDA-MB-468, and the complex had been found to be less cytotoxic to normal cells (Figure S16).

Stability Study by UV−Visible Spectroscopy. It is very fundamental to know how much the metal complex is stable as the therapeutic potential of any compound mostly depends on its stability in the biological environment inside the cell. Therefore, stability of the most potent complex [**L′IrRe**] was studied in 10% DMSO medium (H_2O/DMSO = 9:1) and in 1 mM GSH medium containing PBS buffer as cancer cell possesses high GSH content. In 10% DMSO medium, a minute change in absorbance was found for complex [**L′IrRe**] from 0 h to 12 h of investigation. After that, the absorbance was seen to be almost unchanged from 24 to 72 h of study (Figure S17). This result indicates that the M−Cl bond is slightly labile in nature in less aqueous medium, suggesting the weak tendency to form the aqua complex which can also be validated by the molar conductivity value of this complex in aqueous DMSO. In addition to this, as glutathione (GSH) is known to be a vital detoxifying agent in the presence of GSH S-transferase (GST) in cancer cells, we checked the stability of this complex in excess GSH medium by measuring the change in absorbance with time by dint of UV−visible spectroscopy. The UV−visible spectrum revealed that there was no prominent change in absorbance at all in the presence of GSH. This result signifies that GSH is not competent to deactivate the action of complex [**L′IrRe**] in a subcellular environment. Thus, this complex is extremely stable toward GSH and can easily render its therapeutic action in cancer cells. It is noteworthy that biomolecules also have empathy toward the metal complex as soon as it crosses the plasma membrane of the cell, creating a competition with GSH. However, it was a matter of great pleasure that the complex [**L′IrRe**] was much attuned and readily prone to bind with biomolecules, washing out the probability of competitive binding as GSH was inefficient to bind with the complex. This apparent consequence has been further vindicated from the subsequent binding studies with serum albumin.

DNA Binding Study. Deoxyribonucleic acid (DNA) is considered as the most important pharmacological target for all efficient anticancer metallodrugs like cisplatin, carboplatin, and oxaliplatin and organic drugs like doxorubicin, epirubicin, 5-fluorouracil, and so forth approved by the Food and Drug Administration (FDA) so far. Therefore, a closure look on to the binding efficacy of the metal complexes with DNA provides knowledge of designing fruitful anticancer chemotherapeutics. In order to explore the binding efficacy of synthesized complexes [**L′Re2**], [**L′RuRe**], and [**L′IrRe**] with DNA, we followed the electronic absorption titration method and ethidium bromide (EtBr) displacement assay. The metal complex binds with DNA in two different manners, namely, covalent and non-covalent (electrostatic binding, groove binding, and intercalation). The binding pattern of the complex with DNA can be known from studying the UV−visible spectral arrangement. In order to estimate the equilibrium binding constant (K_b), binding mode, and binding site size (s), all the complexes [**L′Re2**], [**L′RuRe**], and [**L′IrRe**] were titrated with the gradual addition of calf-thymus DNA (ct-DNA, 5−60 μM) to the solutions of the complexes (5×10^{-5} μM). The absorption maxima (λ_{max}) for the complexes [**L′Re2**], [**L′RuRe**], and [**L′IrRe**] were noted at 304, 305, and 306 nm, respectively, in the $\pi-\pi^*$ region. A gradual decrease in intensity of absorption was visualized upon the addition of ct-DNA solution to the stock solution of the complexes (5×10^{-5} μM) with a gradual increase in concentration (5−60 μM), indicating the hypochromism in the $\pi-\pi^*$ region, which suggested the strong intercalative property of these complexes. Hence, these complexes can be ascribed as good DNA intercalators due to substantial planarity of the 2,2′-bipyrimidine ligand (**L′**). The equilibrium binding constant (K_b) values for [**L′Re2**], [**L′RuRe**], and [**L′IrRe**] were evaluated from the linear [DNA]/($\varepsilon_a - \varepsilon_f$) versus [DNA] plots based on the equation (i) (Figure S18). For complex [**L′Re2**], the K_b value was seen to be 0.23×10^5 M^{-1} ($\pi-\pi^*$), for complex [**L′RuRe**], it was 0.26×10^5 M^{-1}($\pi-\pi^*$), and for complex [**L′IrRe**], it was 0.25×10^5 M^{-1} ($\pi-\pi^*$). These experimental K_b values were somewhat lower than the K_b value of EtBr (classical DNA intercalator, $K_{EtBr} = 7 \times 10^5$ M^{-1}). From this study, it was very comprehensible that all the complexes possessed higher binding constants which were comparable to each other, and consequently, complexes [**L′Re2**], [**L′RuRe**], and [**L′IrRe**] attained strong binding aptitude to DNA.

EtBr Displacement Assay. EtBr is renowned to exhibit emission after being incorporated with DNA. Therefore, the competitive binding efficiency of complexes [**L′Re2**], [**L′RuRe**], and [**L′IrRe**] to ct-DNA with respect to EtBr was rationalized by measuring the degree of quenching the fluorescence intensity. Upon constant addition of drugs with increasing concentration (5−60 μM), a gradual decrease in fluorescence intensity was observed as EtBr came out from the EtBr-ct-DNA adduct being displaced by the complexes and

Table 3. Binding Parameters for the Interaction of Complexes [**L′Re2**], [**L′RuRe**], and [**L′IrRe**] with ct-DNA

complex	λ_{max} [nm]	change in absorbance intensity	[a]K_b (M−1)	[b]K_{SV} ($\times 10^6$ M^{-1})	[c]K_{app} ($\times 10^6$ M^{-1})	[d]n
[**L′Re2**]	304	hypochromism	0.23×10^5	0.023	1.8	1.14
[**L′RuRe**]	305	hypochromism	0.26×10^5	0.014	2.0	0.91
[**L′IrRe**]	306	hypochromism	0.25×10^5	0.018	1.6	0.97

[a] k_b, intrinsic DNA binding constant from UV−vis absorption titration. [b] K_{SV}, Stern−Volmer quenching constant. [c] K_{app}, apparent DNA binding constant from competitive displacement. [d] n, binding sites.

free EtBr was non-emissive in nature. Therefore, it can be assumed that these complexes are fervently prone to bind with DNA via intercalation after displacing the stoutly bound EtBr from DNA. In order to obtain the K_{app} values, the concentrations of DNA and EtBr were taken from the literature as [DNA] = 120 μM and [EtBr] = 8 μM, respectively. Then, using equation (iii), the K_{app} values for the complexes [**L′Re2**], [**L′RuRe**], and [**L′IrRe**] were calculated as follows: $K_{app} = 1.8 \times 10^6$ M^{-1} for [**L′Re2**], $K_{app} = 2.0 \times 10^6$ M^{-1} for [**L′RuRe**], and $K_{app} = 1.6 \times 10^6$ M^{-1} for [**L′IrRe**] under 50% quenched conditions, whereas the value of K_{EtBr} is 1.0×10^7 M^{-1} obtained from the literature. The Stern−Volmer quenching constant (K_{SV}) was calculated using eq iv$_a$ (Figure S19), and the values were found to be 0.023×10^6 M^{-1} for [**L′Re2**], 0.014×10^6 M^{-1} for [**L′RuRe**], and 0.018×10^6 M^{-1} for [**L′IrRe**] (Table 3). From the obtained values of binding parameters, it was evident that complex [**L′RuRe**] displayed the highest K_{app}, corroborating the most effective intercalative power of complex [**L′RuRe**] compared to other two complexes. On the other hand, the number of binding sites (n) was calculated as 1.14, 0.91, and 0.97 for complexes [**L′Re2**], [**L′RuRe**], and [**L′IrRe**] respectively (Table 3, eq iv$_b$, and Figure S19).

HSA Binding Study. In order to come across the application of these complexes in the human body, we accentuated the binding study of the complexes [**L′Re2**], [**L′RuRe**], and [**L′IrRe**] with human serum albumin (HSA) following the fluorescence quenching method. The fluorescence spectra of HSA were recorded in the absence and presence of complexes by fixing the excitation wavelength at 300 nm, and hence, the emission was viewed at 405 nm. It was observed that the normal fluorescence intensity of HSA was quenched upon intervallic addition of complexes from 5 to 70, 50, and 55 μM for complexes [**L′Re2**], [**L′RuRe**], and [**L′IrRe**], respectively. The steady decrease in fluorescence intensity indicated that complex molecules were very proficient to bind with HSA, which was clarified by the Stern−Volmer quenching constant (K_{HSA}), quenching rate constant (K_q), and binding constant (K) by applying eqs iv and v (Figure S20). We obtained the values of K_{HSA} as 0.449 × 106 M^{-1} for [**L′Re2**], 0.055×10^6 M^{-1} for [**L′RuRe**], and 0.016×10^6 M^{-1} for [**L′IrRe**]. Then, the value of the bimolecular quenching constant (K_q) was calculated with the help of K_{HSA} and tryptophan life time in HSA ($\tau_0 = 1 \times 10^{-8}$ s), and thereby, we obtained the values of K_q as 4.49×10^{13} M^{-1} S^{-1} for [**L′Re2**], 0.55×10^{13} M^{-1} S^{-1} for [**L′RuRe**], and 0.16×10^{13} M^{-1} S^{-1} for [**L′IrRe**], which were greater than the maximum possible value of the dynamic quenching (2×10^{10} L mol^{-1} s^{-1}) due to molecular collision. Therefore, the experimental K_q values of these complexes implied for the static quenching pathway and the higher order (1013) of the biomolecular quenching constant (K_q) indicated the affluent biomolecular quenching in association with biomolecular binding. Also, the binding affinity (K) and number of binding sites (n) were calculated from the Scatchard plots using eq vi (Figure S20). The binding affinities (K) of complexes [**L′Re2**], [**L′RuRe**], and [**L′IrRe**] were obtained as 1.87 × 104, 2.88 × 104, and 1.24 × 104 M^{-1} respectively. On the other hand, the number of binding sites (n) was calculated as 1.48, 1.12, and 1.16 for complexes [**L′Re2**], [**L′RuRe**], and [**L′IrRe**], respectively (Table 4).

Table 4. Binding Parameters for the Interaction of Complexes [**L′Re2**], [**L′RuRe**], and [**L′IrRe**] with HSA

complex	K_{HSA} $[M^{-1}]$[a]	k_q $[M^{-1}s^{-1}]$[b]	K $[M^{-1}]$[c]	n[d]
[**L′Re2**]	0.449×10^6	4.49×10^{13}	1.87×10^4	1.48
[**L′RuRe**]	0.055×10^6	0.55×10^{13}	2.88×10^4	1.12
[**L′IrRe**]	0.016×10^6	0.16×10^{13}	1.24×10^4	1.16

[a] K_{HSA}, Stern−Volmer quenching constant. [b] K_q, quenching rate constant. [c] K, binding constant with HSA. [d] n, number of binding sites.

Cellular Localization Study. The subcellular localization of the complex [**L′IrRe**] in MDA-MB-468 breast cancer cells was explored using fluorescence microscopy. The complex demonstrated cytoplasmic localization at 25 μM concentration with a green fluorescence emission (Figure S21). The specified breast cancer cells were treated with the complex [**L′IrRe**] and stained with Hoechst and visualized under a fluorescent cell imager, and it was unveiled that complex [**L′IrRe**] was capable of penetrating the cell membrane of MDA-MB-468 breast cancer cells, confirming the subcellular localization of the complex in the cytoplasm but not in the nucleus of the cancer cell. In order to corroborate the mitochondrial localization of the complex [**L′IrRe**], we also performed Mitotracker co-localization assay which revealed the substantial localization of the complex inside the mitochondria of MDA-MB-468 breast cancer cells within 48 h of incubation associated with a good Pearson correlation coefficient of 0.764 (Figure 6).

Owing to the mitochondrial localization of the complex, subsequent experimental validation involved in assessment of mitochondrial membrane potential (MMP) after the administration of complex [**L′IrRe**] by JC-1 staining, detection of DNA damage by γH2Ax staining, and ROS generation detection by DCFDA staining to explore the profound therapeutic potential of this complex like other mitochondria-targeting anticancer compounds.

Mitochondrial Depolarization. JC-1, a cationic carbocyanine dye that accumulates in mitochondria in a potential-dependent manner, was used to reveal changes in mitochondrial membrane potential (MMP, $\Delta\Psi$m) and associated with mitochondrial dysfunction. The positive control for the identification of mitochondrial dysfunction was cells treated with the mitochondrial uncoupler CCCP (carbonyl cyanide *m*-chlorophenylhydrazone), which caused the dissipation of mitochondrial membrane potential (Figure S22).

The flow cytometric measurement of JC-1 stained cells demonstrated that control cells had normal mitochondrial activity without any treatment with ~93% of JC-1 aggregated

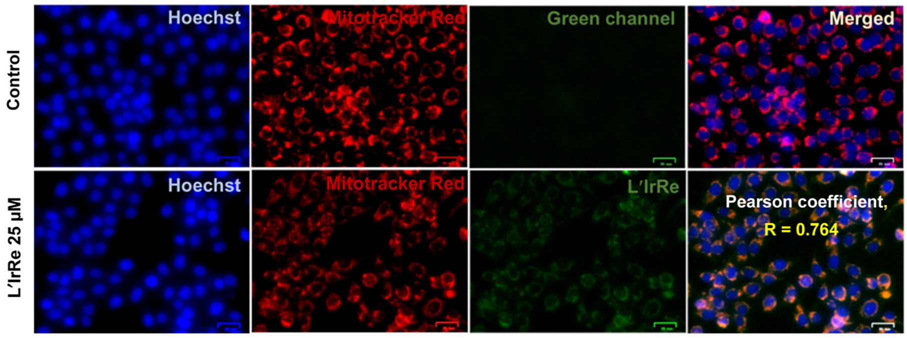

Figure 6. Cytoplasmic localization of the [**L′IrRe**] in MDA-MB-468 cells, with Hoechst co-staining, and a possible mitochondrial localization as indicated by the Mitotracker co-staining. Scale bar, 25 *μ*m.

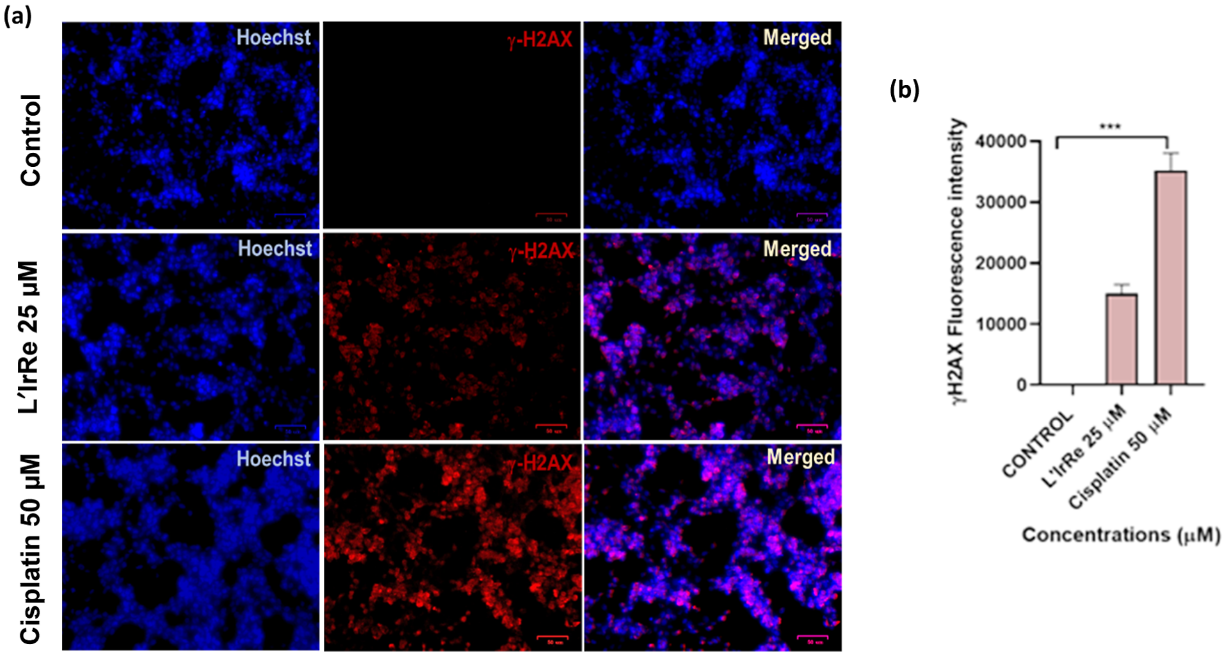

Figure 7. (a) Fluorescence images representing the expression of *γ*H2AX (phosphorylated histone) exhibiting DNA damage in [**L′IrRe**]-treated (25 *μ*M) and cisplatin-treated (50 *μ*M) MDA-MB-468. Untreated control cells are devoid of any DNA damage lacking red fluorescence. Scale bar, 50 *μ*m. (b) Representative graph with the quantification of red fluorescence intensity, indicative of *γ*-H2AX expression.

(red + green fluorescing healthy mitochondria). Only 3.70% of control cells containing JC-1 monomers had impaired mitochondrial activity, displaying green fluorescence (Figure S22B). For the gating purpose, the unstained control shown in Figure S22A was employed. The positive control with CCCP treatment, on the other hand, showed a large percentage of cells (76.98%) with damaged mitochondria, suggesting the existence of green fluorescing JC-1 monomers, compared to 22.08% of cells with healthy mitochondria and red + green fluorescing JC-1 aggregates (Figure S22C). The treatment of [**L′IrRe**] resulted in a dose-dependent increase in JC-1 monomer expressing/green fluorescing cells in MDA-MB-468 cells, indicating damaged mitochondria (Figure S22D−F). At a concentration of 10 *μ*M, the IrL1 complex caused mitochondrial damage in 28.90% of the cells (Figure S22D). However, 25 and 50 *μ*M concentrations of the [**L′IrRe**] complex caused changes in mitochondrial membrane potential and associated damage in a significant proportion of MDA-MB-468 breast cancer cells (30.62 and 62.22%, respectively) (Figure S22E,F). The proportion of green fluorescing JC-1 monomers induced by high concentrations of the complex at 25 and 50 *μ*M concentrations indicates a change in MMP and mitochondrial depolarization, as well as associated mitochondrial dysfunction, leading to a dose-dependent possible cell death mediated by the [**L′IrRe**] complex comparable to the CCCP.

Immunocytochemistry and Detection of DNA Damage by γ-H2AX Staining Assay. The damage of mitochondrial DNA (mtDNA) is also an indication of mitochondrial localization of the complex and a reason of mitochondrial dysfunction following the beginning of apoptosis. To recognize this behavior of the complex [**L′IrRe**], we performed *γ*H2Ax staining of the cells after the treatment of complex [**L′IrRe**]. Subsequently, we analyzed probable DNA damage in the [**L′IrRe**]-treated MDA-MB-468 breast cancer cells by *γ*H2AX staining. The presence of phosphorylated histone mediated by the complex suggested the involvement of the complex [**L′IrRe**] in arbitrating DNA damage (Figure 7) in MDA-MB-468 breast cancer cells. This result concluded that the complex [**L′IrRe**] localized in mitochondria and thereby created mitochondrial DNA damage along with mitochondrial dysfunction.

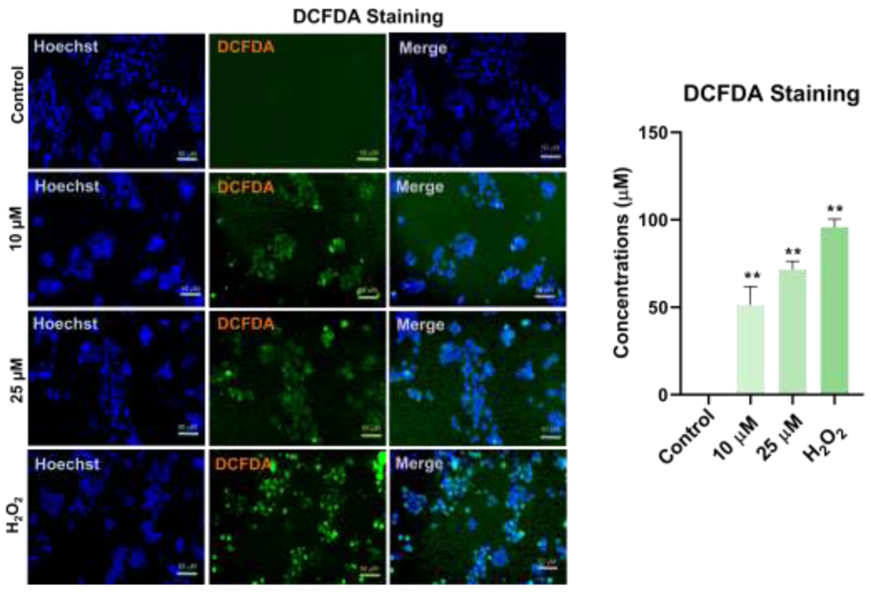

(a) (b)

Figure 8. ROS estimation as a cellular damage measurement after treatment of the MDA-MB468 breast cancer cells with various doses of the [**L′IrRe**] complex and the positive control H_2O_2 in 48 h. (a) ROS detection by DCFDA staining after treatment with [**L′IrRe**] dosages of 10 and 25 and H_2O_2 (positive control). The scale bar is 50 μM. (b) Graph depicting the proportion of DCF-positive cells in MDA-MB-468 breast cancer cells treated with [**L′IrRe**] and H_2O_2 and untreated. 0.001 (**) was the observed *P* value. The error bar represents the ±standard error of mean (SEM).

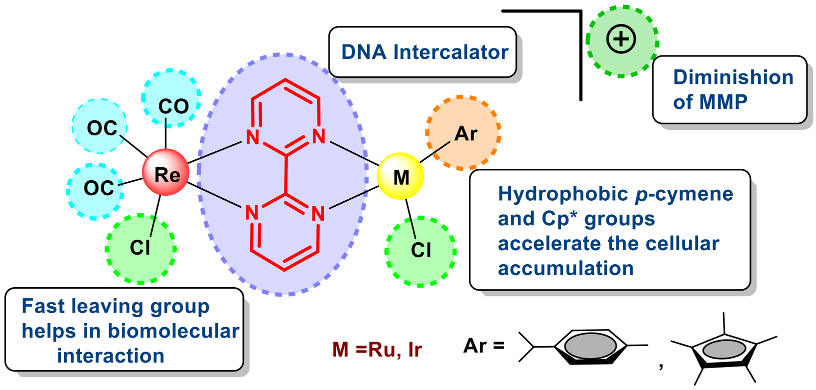

Figure 9. SAR study of 2,2′-bipyrimidine-based Ru(II), Ir(III), and Re(I) mixed metallic complexes [**L′Re**], [**L′RuRe**], and [**L′IrRe**].

Detection of ROS Generation by DCFDA Staining Assay. In MDA-MB-468 breast cancer cells, the [**L′IrRe**] complex produced ROS in a dose-dependent manner, indicating cellular stress and cell death. At the highest tested concentrations of the complex (25 and 50 μM), we observed a dose-dependent increase in ROS generation upon treatment of [**L′IrRe**] in MDA-MB-468 breast cancer cells. The formation of 2′,7′-dichlorofluorescein (DCF) by deacetylation and subsequent oxidation of 2′,7′-dichlorofluorescin diacetate (DCFDA) by cellular esterases and ROS indicated the degree of ROS generation. At 25 μM, the complex produced 49.7% DCF-positive cells, which increased to 73.02% DCF-positive cells at 50 μM concentration. The generation of ROS was not present in the untreated control group. The positive control, on the other hand, exhibits ∼99% of ROS (Figure 8).

Cell Cycle Analysis. Cell cycle analysis was performed to investigate the influence of the [**L′IrRe**] complex on the cell cycle of the MDA-MB-468 breast cancer cell line. Under control circumstances, untreated breast cancer cells showed a high S phase (40.24%), followed by a G2/M phase with 22.18% cells and 33.4% of G0/G1 cells (Figure S23). With the maximum concentration of the complex, 50 μM, the treatment of the complex resulted in a drop of S-phase cells up to 22.14%. Interestingly, the 50 μM concentration significantly enhanced G2/M-phase cells by 42.68%, indicating that the [**L′IrRe**] complex was extremely influential to bring on possible cell death via G2/M cell cycle arrest of MDA-MB-468 breast cancer cells.

Apoptosis in MDA-MB-468 Cells and Annexin FITC/PI Assay. [**L′IrRe**]-treated MDA-MB-468 breast cancer cells showed substantial apoptotic initiation during the annexin FITC/PI assay. At a concentration of 25 μM, 25.42% percent of cells showed the early apoptotic phase, while 4.19% percent showed the late apoptotic phase (Figure S24). The viable cell population was found to be 68.22%. These findings suggested the apoptotic potential of complex [**L′IrRe**] in the TNBC cell line MDA-MB-468.

SAR Study. The SAR study unveiled that the efficacy of 2,2′-bipyrimidine-based Ru (II)/Ir(III)/Re(I) complexes [**L′Re2**], [**L′RuRe**], and [**L′IrRe**] toward triple-negative MDA-MB-468 breast cancer cells varied with the blending of different metals in the bipyrimidine ring. The di-rhenium complex [**L′Re2**] and rhenium−ruthenium complex [**L′RuRe**] showed very low potency, whereas the combination of iridium−rhenium metal elevated the potency of the complex [**L′IrRe**]. Moreover, the complex [**L′IrRe**] was very avid to cause mitochondrial dysfunction through reduction of mitochondrial membrane potential (MMP, $\Delta\Psi$m) due to excellent subcellular accumulation of the concerned complex. The presence of carbonyl (CO) ligands triggered the generation of ROS in association with photophysical properties of iridium metal. Overall results clarified that (i) hydrophobic *p*-cymene and Cp* moieties were eligible to expedite the passive diffusion of the complexes inside the cell, (ii) labile chlorine attached to ruthenium, iridium, and rhenium metals was indispensable for several biomolecular interactions, (iii) Re(I), Ru(II), and Ir(III) complexes enhanced the compound solubility and accelerated the mitochondrial targeting aptitude by reducing the MMP, (iv) bipyrimidine ligand played a vital role as a protagonist in DNA intercalation, (v) the luminescent property of these complexes was beneficial for bioimaging, and (vi) supremacy of the complex [**L′IrRe**] over all the complexes was highlighted with its astounding selectivity in potency possessing the highest lipophilicity, solubility and stability along with significant subcellular accumulation (in mitochondria) reinforced by the synergistic effect of both Re(I) and Ir(III) metals along with the concomitant effect of CO and Cp* groups (Figure 9).

■ CONCLUSIONS

In summary, the meticulous synthesis of three complexes [**L′Re**], [**L′RuRe**], and [**L′IrRe**] had been accomplished, and then, the complexes were subjected to several screenings in order to evaluate their therapeutic potential against TNBC cells using MDA-MB-468 breast cancer cell lines. The light of precise investigations cleared that the cytotoxic capability of the complex [**L′IrRe**] on MDA-MB-468 breast cancer cells was very effective compared to others. The complex [**L′IrRe**] displayed a sparkling binding propensity toward DNA and HSA. The subcellular localization study revealed that the complex was prone to localize in the mitochondria and hence created mitochondrial malfunction. In addition, the profuse production of ROS upon treatment of the complex [**L′IrRe**] pointed out a considerable increase in mitochondrial dysfunction through reduction of mitochondrial membrane potential (MMP) and a steady increase in ROS production and symbolized the excellent mitochondrial targeting capability and substantial mitochondrial accumulation of the complex [**L′IrRe**]. The annexin V-FITC/PI test ratified the lethal ability of the complex [**L′IrRe**] on MDA-MB-468 breast cancer cells by inducing apoptosis which can be most likely as a result of cellular energy stress induced by a higher degree of ROS production. Concomitantly, the [**L′IrRe**] complex played an important role in the G2/M-phase cell cycle arrest in MDA-MB-468 cells at the highest tested concentration of 50 μM. In association with these virtues of that complex, the decent quantum yield (0.0077) can enable it to be employed in bioimaging application. On the other hand, the complex [**L′Re2**] revealed high quantum yield (0.014) and very low toxicity along with good binding efficacy with biomolecules. In a nut shell, it can be presaged that complex [**L′IrRe**] can appear as one of potential therapeutic candidates against TNBC cells in the impending future, while complex [**L′Re2**] can be explored as the best imaging agent for breast cancer.

■ EXPERIMENTAL SECTION

Materials and Methods.[40] The required solvents, reagents, and biochemicals we used in accomplishment of experiments were of paramount commercial excellence. All the reacting ingredients such as bipyrimidine, $[(\eta^5\text{-Cp*})\text{IrCl}(\mu\text{-Cl})]_2$, $[(\eta^6\text{-}p\text{-cymene})\text{RuCl}(\mu\text{-Cl})]_2$, and $\text{Re(CO)}_5\text{Cl}$ were purchased from SPECTROCHEM and from Sigma-Aldrich Chemical Ltd, MERK. HSA, ct-DNA, Mitotracker green, and Hoechst were bought from Sigma-Aldrich Chemical Limited. We obtained triple-negative MDA-MB-468 cell lines from NCCS, Pune. The 10% fetal bovine serum (FBS) was procured from Himidia, and 0.25% trypsin−EDTA was procured from Thermo Fisher Scientific in the USA. Also, 1% penicillin, streptomycin, 1% Glutamax, and DMEM medium were obtained from Gibco Company. The melting points of the complexes were determined with the help of an Elchem microprocessor-based DT apparatus. TLC was performed on silica gel 60 F_{254} precoated aluminum sheets (E. Merck, Germany) using the solvent system hexane, ethylacetate, and methanol, and spots were envisaged under a UV lamp. Infrared (IR) spectroscopy of the complexes was carried out on a Shimadzu Affinity FT-IR spectrometer in the range of 4000−400 cm^{-1}. A 400 MHz Advanced Bruker DPX spectrometer was used to record all the NMR spectra of complexes using tetramethylsilane (TMS) as an internal standard where the chemical shifts were reported in ppm units. Abbreviations are as follows: s, singlet; d, doublet; dd, double doublet; t, triplet; and m, multiplet. The HRMS spectra of the synthesized complexes were recorded on Applied Biosystems (API-4000 ESI-mode) using methanol as the solvent. UV−visible spectra and fluorescence spectra of all the complexes were recorded on a JASCO V-760 spectrometer and Hitachi F7000 fluorescence spectrophotometer, respectively. The conductive property of the complexes was measured using a TDS conductometer. A 96-well plate and ELISA plate reader were used for performing MTT assay.

Synthesis and Characterization of $[(\text{Re}^{\text{I}}(\text{CO})_3\text{Cl})_2(\text{K}^2\text{-}N,N\text{-Bipyrimidine})]$ ([L′Re2]). $\text{Re(CO)}_5\text{Cl}$ (25 mg, 0.069 mmol, 2 equiv) was dissolved in 5 mL of acetonitrile and stirred for 10 min to dissolve the compound completely in acetonitrile. Then, 1.1 equiv of 2,2′-bipyrimidine (**L′**) was added to the reaction mixture and refluxed for 8 h at 80 °C. A change in color from yellow to deep-red was observed, and the progress of the reaction was monitored time to time by TLC using 100% methanol as a solvent system. After the completion of the reaction, acetonitrile was evaporated, and the impurities were removed by washing the crude product thoroughly with 5 mL of hexane followed by diethyl ether. The purified product was further crystalized from methanol/diethyl ether, and the reddish-brown colored fine crystals of complex [**L′Re2**] were obtained with 95% yield. The structure of complex [**L′Re2**] was analyzed by NMR, FT-IR, and HRMS.

*$[(\text{Re}^{\text{I}}(\text{CO})_3\text{Cl})_2(\text{K}^2\text{-}N,N\text{-Bipyrimidine})]$ ([**L′Re2**]).* 51 mg (0.066 mmol, 95%); color: reddish brown; *Mr* ($\text{C}_{14}\text{H}_6\text{N}_4\text{O}_6\text{Cl}_2\text{Re}_2$) = 769.54 g/mol; yield: 95%; mp: 205−208 °C; R_f (100% methanol): 0.38; ^{1}H NMR (DMSO-d_6, 400 MHz): δ 9.33−9.36 (m, 4H, H-1, H-3, H-6, H-8), 7.93 (t, J = 5.2 Hz, 2H, H-2, H-7); ^{13}C NMR (DMSO-d_6, 100 MHz): δ

197.2 (6C, C═O), 161.9 (1C, C-5), 160.6 (1C, C-4), 159.8 (1C, C-1), 150.3 (1C, C-3),146.2 (1C, C-6),139.7 (1C, C-8),127.3 (1C, C-2), 124.9 (1C, C-7); IR (cm^{-1}, KBr): 3328 (Arm C−H stretching), 1884 (C═O stretching), 1574 (Arm C═C stretching), 1413 (C−N stretching), 817 (C−H stretching), 734 (C−H bending); HRMS (MeOH): *m/z*: 770.5486 [M + H]$^+$.

Synthesis and Characterization of [(η^6-*p*-Cymene)-Ru^{II}Re^I(CO)$_3$Cl$_2$(K^2-*N*,*N*-bipyrimidine)]Cl ([L′RuRe]). At first, the mononuclear Ru(II) complex [**L′Ru**] was prepared following the previously reported method.[35] Then, 25 mg (0.069 mmol, 1 equiv) of Re(CO)$_5$Cl was dissolved in 5 mL of acetonitrile and stirred for 10 min to dissolve the compound completely in acetonitrile. After that, the previously prepared complex [**L′Ru**] [(η6-*p*-cymene)RuCl(μ-Cl)]$_2$ was added to the acetonitrile solution. Then, the reaction mixture was refluxed for 8 h, maintaining a temperature of 80 °C. A color change was observed from light orange to dark orange after sometime. Progress of chemical reaction was monitored by TLC using 100% methanol as the solvent system. After the completion of the reaction, acetonitrile was evaporated to obtain the solid product. Then, the crude product was washed thoroughly with hexane followed by diethyl ether two to three times in order to remove the impurities. After washing, the product was dried and weighed in a weighing machine. The purified product was recrystallized from the methanol/diethyl ether system, and brown colored fine crystals were obtained with 95% yield. The structure of [**L′RuRe**] was scrutinized by NMR, FT-IR, and HRMS.

*[(η^6-p-Cymene)Ru^{II}Re^I(CO)$_3$Cl$_2$(K^2-N,N-bipyrimidine)]Cl ([**L′RuRe**]).* 50 mg (0.065 mmol, 95%); color: dark red; *Mr* (C$_{21}$H$_{20}$N$_4$O$_3$Cl$_3$RuRe) = 770.04 g/mol; yield: 95%; mp 225−228 °C; R_f (100% methanol): 0.42; ^{1}H NMR (DMSO-d_6, 400 MHz): δ 9.57 (d, J = 5.6 Hz, 2H), 8.04−8.08 (m, 4H), 6.32 (d, J = 6.4 Hz, 2H, *p*-cymene aromatic-H), 6.09 (d, J = 6.4 Hz, 2H, *p*-cymene aromatic-H), 2.81−2.86 (m, 1H, *p*-cymene CH), 2.15 (s, 3H, *p*-cymene Me), 1.20 (d, J = 6.8 Hz, 6H, *p*-cymene isopropyl CH$_3$); ^{13}C NMR (DMSO-d_6, 100 MHz): δ197.2 (3C, C═O), 161.9 (1C, C-5), 160.7 (1C, C-4), 149.9 (1C, C-1), 141.7 (1C, C-3), 124.9 (1C, C-6), 121.2 (1C, C-8), 115.5 (1C, C-2), 110.9 (1C, C-7), 103.5 (*p*-cymene), 102.9 (*p*-cymene), {86.8, 86.5, 85.9, 84.9} (*p*-cymene, 4-aromatic CH), 30.5 (*p*-cymene, aliphatic CH), {22.3, 21.9} (*p*-cymene, isopropyl CH$_3$), 18.2 (*p*-cymene, methyl CH$_3$); IR (cm^{-1}, KBr): 3065 (ArmC-H stretching), 1884 (C═O stretching), 1578 (Arm C═C stretching), 1410 (C−N stretching), 1146 (C−H stretching), 733 (C−H bending); HRMS (MeOH): *m/z*: 734.5915 [M−Cl]$^+$.

Synthesis and Characterization [(η^5-Cp*)-Ir^{III}Re^I(CO)$_3$Cl$_2$(K^2-*N*,*N*-Bipyrimidine)]Cl ([L′IrRe]). At first, the mononuclear Ir(III) complex [**L′Ir**] was prepared following the previous method.[35] Then, 25 mg (0.069 mmol, 1 equiv) of Re(CO)$_5$Cl was dissolved in 5 mL of acetonitrile along with the addition of 1.1 equiv of complex [**L′Ir**], and the reaction mixture was stirred for 10 min to dissolve the compounds completely in acetonitrile. Then, the reaction mixture was subjected to keep under reflux conditions for 8 h at 80 °C. The progress of the reaction was monitored time to time using TLC in 100% methanol as the solvent system. After completion of the reaction, the solvent was evaporated and the obtained crude product was completely dried followed by washing with hexane 6 to 10 times to remove impurities. After washing, the product was dried, and then, the purified product was recrystallized from methanol/diethyl ether to obtain the yellow colored fine crystals of complex [**L′IrRe**]. The product was then weighed in a weighing machine, and the yield was 96%. The structure of [**L′IrRe**] was analyzed by NMR, FT-IR, and HRMS.

[(η^5-Cp)Ir^{III}Re^I(CO)$_3$Cl$_2$(K^2-N,N-Bipyrimidine)]Cl ([**L′IrRe**]).* 57 mg (0.066 mmol, 96%); color: yellow; *Mr* (C$_{21}$H$_{21}$N$_4$O$_3$Cl$_3$IrRe) = 862.20 g/mol; yield: 96%; mp: 235−237 °C; R_f (100% methanol): 0.46; ^{1}H NMR (DMSO-d_6, 400 MHz): δ 9.32−9.36 (m, 3H), 8.05 (t, J = 5.2 Hz), 7.93 (t, 2H), 1.62 (s, 15H, Cp*); ^{13}C NMR (DMSO-d_6, 100 MHz): δ197.5 (3C, C═O), 161.9 (1C, C-5), 160.9 (1C, C-4), 159.6 (1C, C-1), 150.3 (1C, C-3), 142.5 (1C, C-6),133.1 (1C, C-8), 127.2 (1C, C-2), 116.1 (1C, C-7), {92.6, 90.3} (Cp*, 5C, aromatic ring), {8.7, 8.6} (Cp*, 5C, CH$_3$); IR (cm^{-1}, KBr): 3359 (Arm C−H stretching), 1896 (C═O stretching), 1578 (Arm C═C stretching), 1410 (C−N stretching), 1020 (C−H stretching), 733 (C−H bending); HRMS(MeOH): *m/z*: 826.7466 [M−Cl]$^+$.

Biology. *Cytotoxicity Study.* Cytotoxicity study of all the synthesized complexes was performed against TNBC cells (MDA-MB-468) and immortalized human keratinocyte cell line HaCaT incubating the complex over a period of 48 h following the standard procedure stated in the Supporting Information. Preliminary studies were executed to understand the mode of action of each complex to induce cytotoxicity using flow cytometric methods.

Mitochondrial Membrane Dysfunction Assay. JC-1, a cationic carbocyanine dye, was used to validate the variations in mitochondrial membrane potential (MMP, ΔΨm) in association with the mitochondrial dysfunction. The cells were treated with the mitochondrial uncoupler CCCP (carbonyl cyanide *m*-chlorophenylhydrazone) as the positive control, which facilitated the dissipation of mitochondrial membrane potential. The flow cytometric quantification of JC-1 stained cells revealed a normal mitochondrial function in control cells, and the results obtained from the quantified JC-1 stained cells among [**L′IrRe**]-treated cells were compared with the same of the control.

Imaging Studies. Colocalization study and ROS generation studies were performed using live cell lines in their log phase.

Statistical Analysis. As the study had more than one group, one-way ANOVA was used for statistical analysis. The p value < 0.05 was considered as significant.

■ ASSOCIATED CONTENT

Supporting Information

The Supporting Information is available free of charge at https://pubs.acs.org/doi/10.1021/acsomega.2c08285.

^{1}H and ^{13}C NMR, FT-IR, HRMS, UV−vis, and fluorescence spectra of all complexes (PDF)

■ AUTHOR INFORMATION

Corresponding Authors

Bipasha Bose − *Department Stem Cells and Regenerative Medicine Centre, Institution Yenepoya Research Centre, Yenepoya University, Mangalore 575018 Karnataka, India;* Email: bipasha.bose@gmail.com

Vijayaraghavan Rajagopalan − *Department of Chemistry, School of Advanced Sciences, Vellore Institute of Technology, Vellore 632014 Tamilnadu, India;* orcid.org/0000-0001-9004-6077; Email: rvijayaraghavan@vit.ac.in

Priyankar Paira − *Department of Chemistry, School of Advanced Sciences, Vellore Institute of Technology, Vellore 632014 Tamilnadu, India*; orcid.org/0000-0003-1698-4895; Email: priyankar.paira@vit.ac.in

Authors

Nilmadhab Roy − *Department of Chemistry, School of Advanced Sciences, Vellore Institute of Technology, Vellore 632014 Tamilnadu, India*

Shanooja Shanavas − *Department Stem Cells and Regenerative Medicine Centre, Institution Yenepoya Research Centre, Yenepoya University, Mangalore 575018 Karnataka, India*

Binoy Kar − *Department of Chemistry, School of Advanced Sciences, Vellore Institute of Technology, Vellore 632014 Tamilnadu, India*; orcid.org/0000-0002-2059-6900

Lavanya Thilak Babu − *Department of Chemistry, School of Advanced Sciences, Vellore Institute of Technology, Vellore 632014 Tamilnadu, India*

Utpal Das − *Department of Chemistry, School of Advanced Sciences, Vellore Institute of Technology, Vellore 632014 Tamilnadu, India*

Seshu Vardhan − *Department of Applied Chemistry, S.V. National Institute of Technology (SVNIT), Surat, Gujarat 395007, India*; orcid.org/0000-0002-8906-5243

Suban K. Sahoo − *Department of Applied Chemistry, S.V. National Institute of Technology (SVNIT), Surat, Gujarat 395007, India*; orcid.org/0000-0003-1751-5310

Complete contact information is available at:
https://pubs.acs.org/10.1021/acsomega.2c08285

Author Contributions

[‖]N.R., S.S., and B.K. contributed equally.

Notes

The authors declare no competing financial interest.

ACKNOWLEDGMENTS

Authors are grateful to the Department of Science and Technology, Government of India, for supporting their work through the DST-SERB CRG project grant (CRG/2021/002267). The authors are grateful to VIT University for providing VIT SEED funding. The authors acknowledge DST, New Delhi, India, for DST-FIST project.

ABBREVIATIONS

NMR	nuclear magnetic resonance
HRMS	high-resolution mass spectrometry
ppm	parts per million
LLCT	ligand−ligand charge transfer
MLCT	metal to ligand charge transfer
MTT	3-(4,5-dimethylthiazol-2-yl)-2,5-diphenyltetrazolium bromide
GSH	glutathione
TLC	thin-layer chromatography
s	singlet
d	doublet
brs	broad singlet
t	triplet
m	multiplet
OD	optical density
ct-DNA	calf-thymus DNA
HSA	human serum albumin
EtBr	ethidium bromide
DFT	density functional theory
K_b	intrinsic binding constant
K_{sv}	Stern−Volmer quenching constant
K_{app}	apparent binding constant
K	overall binding constant

REFERENCES

(1) Atoui, A.; Bou Zerdan, M. B.; El Mahmoud, A. E.; Chamseddine, N.; Hamad, L.; Assi, H. I. Clinical Significance of Breast Cancer Molecular Subtypes and Ki67 Expression as a Predictive Value for Pathological Complete response following Neoadjuvant Chemotherapy: Experience from a Tertiary Care Center in Lebanon. *Int. J. Breast Cancer* **2022**, *2022*, 1218128.

(2) Medina, M. A.; Oza, G.; Sharma, A.; Arriaga, L. G.; Hernández Hernández, J. M. H.; Rotello, V. M.; Ramirez, J. T. Triple-Negative Breast Cancer: A Review of Conventional and Advanced Therapeutic Strategies. *Int. J. Environ. Res. Publ. Health* **2020**, *17*, 2078.

(3) Ghoncheh, M.; Pournamdar, Z.; Salehiniya, H. Incidence and mortality and epidemiology of breast cancer in the world. *Asian Pac. J. Cancer Prev. APJCP* **2016**, *17*, 43−46.

(4) Oeffinger, K. C.; Fontham, E. T. H.; Etzioni, R.; Herzig, A.; Michaelson, J. S.; Shih, Y.-C.; Walter, L. C.; Church, T. R.; Flowers, C. R.; LaMonte, S. J.; Wolf, A. M. D.; DeSantis, C.; Lortet-Tieulent, J.; Andrews, K.; Manassaram-Baptiste, D.; Saslow, D.; Smith, R. A.; Brawley, O. W.; Wender, R. Breast Cancer Screening for Woman at Average Risk 2015 Guideline Update From the American Cancer Society. *J. Am. Med. Assoc.* **2015**, *314*, 1599−1614.

(5) Domínguez-Martís, E. M.; Mosteiro-Miguéns, D. G.; Vigo-Gendre, L.; López-Ares, D.; Freire-Garabal, M.; Núñez-Iglesias, M. J.; Novío, S. Non-Platinum Metal Complexes as Potential Anti-Triple Negative Breast Cancer Agents. *Crystals* **2018**, *8*, 369.

(6) Watkins, E. J. Overview of breast cancer. *J. Am. Acad. Physician Assist.* **2019**, *32*, 13−17.

(7) Golbaghi, G.; Castonguay, A. Rationally Designed Ruthenium Complexes for Breast Cancer Therapy. *Molecules* **2020**, *25*, 265.

(8) Furlanetto, J.; Loibl, S. Optimal Systemic Treatment for Early Triple-Negative Breast Cancer. *Breast Cancer* **2020**, *15*, 217−226.

(9) Li, Y.; Liu, B.; Shi, H.; Wang, Y.; Sun, Q.; Zhang, Q. Metal complexes against breast cancer stem cells. *Dalton Trans.* **2021**, *50*, 14498−14512.

(10) Liao, M.; Qin, R.; Huang, W.; Zhu, H. P.; Peng, F.; Han, B.; Liu, B. Targeting regulated cell death (RCD) with small-molecule compounds in triple-negative breast cancer: a revisited perspective from molecular mechanisms to targeted therapies. *J. Hematol. Oncol.* **2022**, *15*, 44.

(11) Tarantino, P.; Corti, C.; Schmid, P.; Cortes, J.; Mittendorf, E. A.; Rugo, H.; Tolaney, S. M.; Bianchini, G.; Andrè, F.; Curigliano, G. Immunotherapy for early triple negative breast cancer: research agenda for the next decade. *Breast Cancer* **2022**, *8*, 23.

(12) Nayeem, N.; Contel, M. Exploring the Potential of Metallodrugs as Chemotherapeutics for Triple Negative Breast Cancer. *Chem.—Eur. J.* **2021**, *27*, 8891−8917.

(13) Shumi, G.; Desalegn, T.; Demissie, T. B.; Ramachandran, V. P.; Eswaramoorthy, R. Metal Complexes in Target-Specific Anticancer Therapy: Recent Trends and Challenges. *J. Chem.* **2022**, *2022*, 9261683.

(14) Wang, H.; Guo, S.; Kim, S.-J.; Shao, F.; Ho, J. W. K.; Wong, K. U.; Miao, Z.; Hao, D.; Zhao, M.; Xu, J.; Zeng, J.; Wong, K. H.; Di, L.; Wong, A. H.-H.; Xu, X.; Deng, C.-X. Cisplatin prevents breast cancer metastasis through blocking early EMT and retards cancer growth together with paclitaxel. *Theranostics* **2021**, *11*, 2442−2459.

(15) Ciarimboli, G. Membrane transporters as mediators of cisplatin side-effects. *Anticancer Res.* **2014**, *34*, 547−550.

(16) Golbaghi, G.; Haghdoost, M. M.; Yancu, D.; López de los Santos, Y. L.; Doucet, N.; Patten, S. A.; Sanderson, J. T.; Castonguay, A. Organoruthenium(II) Complexes Bearing an Aromatase Inhibitor:

Synthesis, Characterisation, *in Vitro* Biological Activity and *in Vivo* Toxicity in Zebrafish Embryos. *Organometallics* **2019**, *38*, 702−711.

(17) Lida, J.; Bell-Loncella, E. T.; Purazo, M. L.; Lu, Y.; Dorchak, J.; Clancy, R.; Slavik, J.; Cutler, M. L.; Shriver, C. D. Inhibition of cancer cell growth by ruthenium complexes. *J. Transl. Med.* **2016**, *14*, 48.

(18) Popolin, C. P.; Reis, J. P. B.; Becceneri, A. B.; Graminha, A. E.; Almeida, M. A. P.; Corrêa, R. S.; Colina-Vegas, L. A.; Ellena, J.; Batista, A. A.; Cominetti, M. R. Cytotoxicity and anti-tumor effects of new ruthenium complexes on triple negative breast cancer cells. *PLoS One* **2017**, *12*, No. e0183275.

(19) Chen, Q.; He, L.; Li, X.; Xu, L.; Chen, T. Ruthenium complexes boost NK cell immunotherapy via sensitizing triple-negative breast cancer and shaping immuno-microenvironment. *Biomaterials* **2022**, *281*, 121371.

(20) Grawe, G. F.; Oliveira, K. M.; Leite, C. M.; de Oliveira, T. D.; Honorato, J.; Ferreira, A. G.; Castellano, E. E.; Cominetti, M. R.; Correa, R. S.; Batista, A. A. Ruthenium (II)-diphosphine complexes containing acylthiourea ligands are effective against lung and breast cancers. *Dalton Trans.* **2022**, *51*, 1489−1501.

(21) Ma, D.-L.; Wu, C.; Wu, K. J.; Leung, C.-H. Iridium(III) Complexes Targeting Apoptotic Cell Death in Cancer Cells. *Molecules* **2019**, *24*, 2739.

(22) Hearn, J. M.; Romero-Canelón, I.; Qamar, B.; Liu, Z.; Hands-Portman, I.; Sadler, P. J. Organometallic Iridium (III) Anticancer Complexes with New Mechanisms of Action: NCI-60 Screening, Mitochondrial Targeting and Apoptosis. *ACS Chem. Biol.* **2013**, *8*, 1335−1343.

(23) Sun, Q.; Wang, Y.; Fu, Q.; Ouyang, A.; Liu, S.; Wang, Z.; Su, Z.; Song, J.; Zhang, Q.; Zhang, P.; Lu, D. Sulfur-Coordinated Organiridium(III) Complexes Exert Breast Anticancer Activity via Inhibition of Wnt/β-Catenin Signaling. *Angew. Chem.* **2020**, *133*, 4891−4898.

(24) Wang, W.-J.; Ling, Y.-Y.; Zhong, Y.-M.; Li, Z. Y.; Tan, C.-P.; Mao, Z.-W. Ferroptosis-Enhanced Cancer Immunity by a Ferrocene-Appended Iridium(III) Diphosphine Complex. *Angew. Chem.* **2022**, *61*, No. e202115247.

(25) Konkankit, C. C.; King, A. P.; Knopf, K. M.; Southard, T. L.; Wilson, J. J. In Vivo Anticancer Activity of a Rhenium (I) Tricarbonyl Complex. *ACS Med. Chem. Lett.* **2019**, *10*, 822−827.

(26) Pan, Z.-Y.; Cai, D.-H.; He, L. Dinuclear phosphorescent rhenium (I) complexes as potential anticancer and photodynamic therapy agents. *Dalton Trans.* **2020**, *49*, 11583−11590.

(27) Bauer, E. B.; Haase, A. A.; Reich, R. M.; Crans, D. C.; Kühn, F. E. Organometallic and Coordination rhenium compounds and their potential in cancer therapy. *Coord. Chem. Rev.* **2019**, *393*, 79−117.

(28) Subasinghe, A.; Perera, I. C.; Pakhomova, S.; Perera, T. Synthesis, Characterization and Biological Studies of a Piperidinyl Appended Dipicolylamine Ligand and Its Rhenium Tricarbonyl Complex as Potential Therapeutic Agents for Human Breast Cancer. *Bioinorg. Chem. Appl.* **2016**, *2016*, 2675937.

(29) Knopf, K. M.; Murphy, B. L.; MacMillan, S. N.; Baskin, J. M.; Barr, M. P.; Boros, E.; Wilson, J. J. In Vitro Anticancer Activity and in Vivo Biodistribution of Rhenium (I) Tricarbonyl Aqua Complexes. *J. Am. Chem. Soc.* **2017**, *139*, 14302−14314.

(30) Schindler, K.; Zobi, F. Anticancer and Antibiotic Rhenium Tri- and Dicarbonyl Complexes: Current Research and Future Perspectives. *Molecules* **2022**, *27*, 539.

(31) Altaf, M.; Casagrande, N.; Mariotto, E.; Baig, N.; Kawde, A.-N.; Corona, G.; Larcher, R.; Borghese, C.; Pavan, C.; Seliman, A. A.; Aldinucci, D.; Isab, A. A. Potent In Vitro and In Vivo Anticancer Activity of New Bipyridine and Bipyrimidine Gold (III) Dithiocarbamate Derivatives. *Cancers* **2019**, *11*, 474−488.

(32) Kumar, S.; Narasimhan, B. Therapeutic potential of heterocyclic pyrimidine scaffolds. *Chem. Cent. J.* **2018**, *12*, 38.

(33) Mahapatra, A.; Prasad, T.; Sharma, T. Pyrimidine: a review on anticancer activity with key emphasis on SAR. *Future J. Pharm. Sci.* **2021**, *7*, 123.

(34) Tylińska, B.; Wiatrak, B.; Czyznikowska, Z.; Ciesla-Niechwiadowicz, A.; Gebarowska, E.; Janicka-Klos, A. Novel Pyrimidine Derivatives as Potential Anticancer Agents: Synthesis, Biological Evaluation and Molecular Docking Study. *Int. J. Mol. Sci.* **2021**, *22*, 3825.

(35) Roy, N.; Sen, U.; Moharana, P.; Babu, L.; Kar, B.; Vardhan, S.; Sahoo, S. K.; Bose, B.; Paira, P. 2, 2″- Bipyrimidine-based luminescent Ru(II)/Ir(III)-arene monometallic and homo- and hetero-bimetallic complexes for therapy against MDA-MB-468 and Caco-2 cells. *Dalton Trans.* **2021**, *50*, 11725.

(36) Kubanik, M.; Holtkamp, H.; Söhnel, T.; Jamieson, S. M. F.; Hartinger, C. G. Impact of the Halogen Substitution Pattern on the Biological Activity of Organoruthenium 8-Hydroxyquinoline Anticancer Agents. *Organometallics* **2015**, *34*, 5658−5668.

(37) Frisch, M. J.; Trucks, G. W.; Schlegel, H. B.; Scuseria, G. E.; Robb, M. A.; Cheeseman, J. R.; Scalmani, G.; Barone, V.; Mennucci, B.; Petersson, G. A. et al. *Gaussian 09W*; Gaussian, Inc.: Wallingford CT, 2009.

(38) Morris, G. M.; Huey, R.; Lindstrom, W.; Sanner, M. F.; Belew, R. K.; Goodsell, D. S.; Olson, A. J. AutoDock4 and AutoDockTools4: Automated docking with selective receptor flexibility. *J. Comput. Chem.* **2009**, *30*, 2785−2791.

(39) Patra, S.; Santhosh, K.; Pabbathi, A.; Samanta, A. Diffusion of organic dyes in bovine serum albumin solution studied by fluorescence correlation spectroscopy. *RSC Adv.* **2012**, *2*, 6079−6086.

(40) Mondal, A.; Shanavas, S.; Sen, U.; Das, U.; Roy, N.; Bose, B.; Paira, P. Mitochondria-targeted half-sandwich iridium(III)-Cp*-arylimidazophenanthroline complexes as antiproliferative and bio-imaging agents against triple negative breast cancer cells MDA-MB-468. *RSC Adv.* **2022**, *12*, 11953−11966.